Composites Science and Technology 257 (2024) 110824

Contents lists available at ScienceDirect

Composites Science and Technology

journal homepage: www.elsevier.com/locate/compscitech

Effect of adhesive ductility on the bond behavior of CFRP-steel cohesive interfaces made with toughened epoxy resin

Angelo Savio Calabrese, Tommaso D'Antino *, Pierluigi Colombi

Department of Architecture, Built Environment and Construction Engineering, Politecnico Milano 1863, P.zza L. da Vinci, 32, 20133, Milan, Italy

ARTICLE INFO

Handling Editor: Ming-Qiu Zhang

Keywords:
CFRP
Steel
Debonding
Cohesive material law
Snap-back

ABSTRACT

The strengthening of steel structures can be effectively performed using carbon fiber-reinforced polymers (CFRP) plates. Specifically, the behavior of corroded and fatigue damaged steel bridges can be significantly improved using externally bonded (EB) or unbonded composite reinforcements. For bonded composites, the bond between the reinforcement and the steel substrate is the weak link of the system. Indeed, cohesive failure within the adhesive layer represents the main failure mode, which makes the selection of a proper adhesive fundamental to achieve an improvement of the system load carrying capacity and fatigue resistance. Within this context, the use of toughened adhesives represents a promising solution. However, research regarding these adhesives is still limited. In this paper, 18 single-lap direct shear tests are performed to evaluate the cohesive behavior of toughened and traditional adhesives. For some specimens, the full-range bond behavior, including the load response snap-back, was experimentally captured. The digital image correlation (DIC) technique is adopted to evaluate the adhesives cohesive material law (CML). The effect of adhesive ductility, plate stiffness, and bonded length on the joint load response is investigated. Finally, experimental results are validated and discussed against the analytical predictions of a cohesive model based on a trapezoidal CML.

1. Introduction

Strengthening and retrofitting with fiber-reinforced polymer (FRP) plates represent a valid alternative to traditional methods for the local reinforcement of existing structural members [1]. FRP plates are industrially-made unidirectional composites including high strength fibers (e.g., carbon, glass, and basalt) impregnated with epoxy resin, typically realized by pultrusion [2]. Pultruded FRP plates have controlled fiber and matrix volume fractions, aligned fibers, and are industrially pre-cured, which makes their application easy and fast.

Both externally bonded (EB) and unbonded carbon FRP (CFRP) applications reportedly increase the structural capacity of corroded and fatigue-damaged steel bridges [3,4]. For these structures, high modulus fibers are required due to the high Young's modulus of the steel substrate. CFRP strips could be prestressed to achieve an additional decrement of the crack propagation rate, leading eventually to crack arrest [4]. Pre-stressing can be also achieved using thermally activated shape memory alloy wires embedded within the CFRP plates [5,6].

One of the main issues related with EB CFRP strengthening is the occurrence of composite debonding, which makes bond between the CFRP plate and the steel substrate a key feature of the system [7]. Debonding could occur within the adhesive layer (cohesive debonding), at the composite-adhesive interface or at the steel-adhesive interface, and within the composite (composite delamination) [8]. Note that debonding never affects the steel substrate. Cohesive debonding can be considered as a ductile phenomenon and thus as the ideal failure mode. Proper preparation of the steel substrate could avoid the steel-adhesive interface debonding [9–12], which is instead a brittle and then undesirable phenomenon. Debonding at the composite-adhesive interface, which is again a brittle phenomenon, can be avoided properly selecting the composite and adhesive type and preparing the reinforcement surface. Finally, composite delamination [13,14], which is a ductile and then acceptable failure mode, can be avoided by a proper design of geometrical and mechanical properties of the CFRP plate. Debonding can be induced either by in-plane shear stresses in the adhesive joint (i.e., pure Mode-II fracture mechanics loading condition) or by combined in- and out-of-plane stresses, such as in the case of a peeling component normal to the joint plane (i.e., mixed Mode-I/II loading condition). To avoid the detrimental effect of the peeling stresses on the composite bond, mechanical anchorages were applied at the reinforcement end or

* Corresponding author.
E-mail address: tommaso.dantino@polimi.it (T. D'Antino).

https://doi.org/10.1016/j.compscitech.2024.110824
Received 20 April 2024; Received in revised form 14 August 2024; Accepted 20 August 2024
Available online 22 August 2024

at material or geometrical discontinuities [15].

When debonding occurs within the adhesive layer, a cohesive approach can be adopted. Both pure Mode-II and mixed Mode-I/II loading conditions can be investigated by introducing a τ-s and σ-w law, respectively, referred to as cohesive material laws (CML). They relate the shear stress τ and the peeling stress σ to the slip s and crack opening w, respectively, which are the relative in-plane and out-of-plane displacements between the adherends. Analytical [8,16,17] and numerical cohesive approaches [18–20] were developed to investigate the load-slip response of the cohesive interface of EB CFRP reinforcement subjected to direct shear. Recently, a cohesive analytical model presented by the authors [21], which utilized a trapezoidal CML to depict the stress-slip behavior of toughened adhesives, was found to accurately predict the load response of CFRP-steel joints experiencing cohesive debonding within the toughened adhesive layer. Cohesive approaches were also successfully used for the investigation of the fatigue behavior of CFRP-steel interfaces under fatigue loading [6,22–24]. This model was shown to be effective in predicting the joint bond capacity. However, when the joint bonded length is higher than the effective bond length (i.e., the minimum length required to allow the full transfer of the bond shear stress [21]), the post-peak stage of the analytical load response shows a snap-back that is not captured in corresponding displacement (stroke) controlled experimental direct-shear tests. The load response snap-back is due to the elastic energy release of the debonded portion of the joint that, when the applied load decreases, recovers its elastic deformation causing a decrease of the relative slip between the two adherends at the joint loaded end.

The bond behavior under monotonic load of CFRP-steel joints with different adhesive types was investigated experimentally by several authors in the literature [7,18,25,26]. The fatigue behavior was also studied [27,28]. The traditional epoxy adhesives [7,18,25], usually referred to as brittle adhesives, were characterized by linear elastic stress-strain behavior and brittle tensile failure. A new type of epoxy adhesives, referred to as ductile or toughened adhesives [7,25,26,29], showed a nonlinear stress-strain tensile behavior with elastic modulus and failure stress lower than those of brittle adhesives. However, they provided elongation at failure significantly larger than those of brittle adhesives. Brittle adhesives presented a limited ability to allow stable crack propagation before failure, which was responsible for the limited quasi-static bond capacity (i.e., the maximum applied load provided by bond only) and resistance to dynamic actions such as impacts and cyclic loading. Conversely, ductile adhesives showed a fracture toughness higher than that of brittle adhesives, which was responsible for the high bond capacity (and interface fracture energy). To investigate the bond behavior of adhesively bonded CFRP-steel joints with a ductile adhesive, Yu et al. [30] conducted an experimental campaign comprising single-lap direct shear tests with brittle and ductile adhesives. The results showed that ductile adhesives were characterized by a nonlinear stress-strain behavior with larger ultimate tensile strain than brittle adhesives. This determined higher bond capacity and ductility for the joints with ductile than with brittle adhesives. He and Xian [18] experimentally studied CFRP-steel joints using a single shear lap joint and a brittle adhesive. A CML was also proposed based on the experimental outcomes and used in finite element simulations. In Wang and Wu [25], both brittle and ductile adhesives were compared and expressions for the key parameters adopted in the bilinear (brittle adhesive) and trilinear (ductile adhesive) CML were proposed. In Wang et al. [26], single shear lap tests were used to investigate the bond of CFRP-steel joints with a ductile adhesive. Three-dimensional digital image correlation (DIC) was used to measure the CFRP axial strain distribution and a trilinear shape of the CML was proposed.

Recent literature showed that rubber-like toughened adhesives [31] can be efficiently used for the strengthening of steel structures subjected to dynamic actions, such as steel bridges. The rubber-like particles increase the material toughness by plastic void growth, localized plastic deformation, and crack bridging [32]. All these mechanisms entail for energy dissipation that enhances the fracture toughness. This is particularly effective under fatigue or dynamic loading since the growth of micro cracks inside the matrix is delayed by the higher energy required for crack propagation [33]. A two-component toughened epoxy adhesive for the strengthening of fatigue-sensitive steel structures was proposed in Ref. [34] and its application with CFRP plates to a steel substrate was investigated in Ref. [33]. The results showed that high toughness improved the fatigue resistance of the adhesive joint without affecting its long term deformation (creep) capacity [34]. Fatigue tests on center-cracked steel elements strengthened with EB CFRP plates using the toughened adhesive showed an increase of residual lifetime of a maximum of 7.9 times compared to unreinforced specimens. This was attributed to the capacity of the CFRP plate to reduce both the crack tip stress and the crack growth rate [34].

In this paper, the bond behavior of adhesively bonded CFRP-steel joints made with a toughened adhesive is investigated and compared with that of nominally equal joints with a traditional adhesive. The parameters studied are the adhesive ductility, CFRP plate stiffness, and bonded length. A trapezoidal CML is used with an analytical cohesive model to describe the load responses obtained experimentally. The results discussed in this paper represent the first attempt to provide a description of the full-range bond behavior of CFRP-steel joints with a toughened adhesive and provide fundamental indications on the features of the CML that describes the bond behavior observed.

2. Research significance

In this study, the bond behavior of adhesively bonded CFRP-steel joints made with a toughened adhesive is investigated and compared with that of a traditional adhesive. First, in Section 3 the mechanical properties of the composite plate and of the adhesive are experimentally investigated by tensile tests. After describing the experimental set-up (Section 4), results of single-lap direct shear tests on CFRP-steel joints are provided and discussed in Section 5. For some sufficiently long bonded lengths, tests are performed controlling the slip at different locations along the bonded length to capture the full-range bond behavior of the joint, including the snap-back branch. In Section 6, the joint interfacial axial strain and slip distributions measured with the DIC technique are presented. In Section 7, the experimental findings are finally validated and discussed against the analytical predictions of a trapezoidal cohesive model previously presented by the authors [21], allowing to define a closed-form analytical estimation of the effective bond length. The effect of adhesive ductility, plate stiffness, and bonded length on the joint load response are also investigated and discussed.

3. Materials

Two different CFRP plates were considered in this study and were named type M [35] and type S [36]. Both CFRP composites were comprised of unidirectional carbon fibers impregnated with epoxy matrix and had a fiber volume fraction of 68 % and nominal thickness $t_f =$ 1.4 mm. The type M composite had a higher elastic modulus and tensile strength than the type S. The mechanical properties of the CFRP plates were obtained by tensile testing of three rectangular specimens of nominal dimensions 25 mm (width) × 250 mm (height), according to ISO 527–4 [37] (Fig. 1a).

Tests were conducted in displacement control mode, at a rate of 2 mm/min, while the axial strain was measured using an extensometer with a gauge length of 50 mm. The stress-strain response of each specimen is shown in Fig. 1b. Table 1 reports the average CFRP elastic modulus E_f, ultimate tensile stress $\sigma_{f,u}$, and corresponding strain $\varepsilon_{f,u}$. E_f was computed by linear regression of points of the stress-strain curves between $0.2\sigma_{f,u}$ and $0.5\sigma_{f,u}$. The extensometer was removed from the specimen at approximately 60 % of the maximum expected load to prevent possible damage caused by the specimen failure. Accordingly, $\varepsilon_{f,u}$ reported in Table 1 was obtained as the ratio between $\sigma_{f,u}$ and E_f.

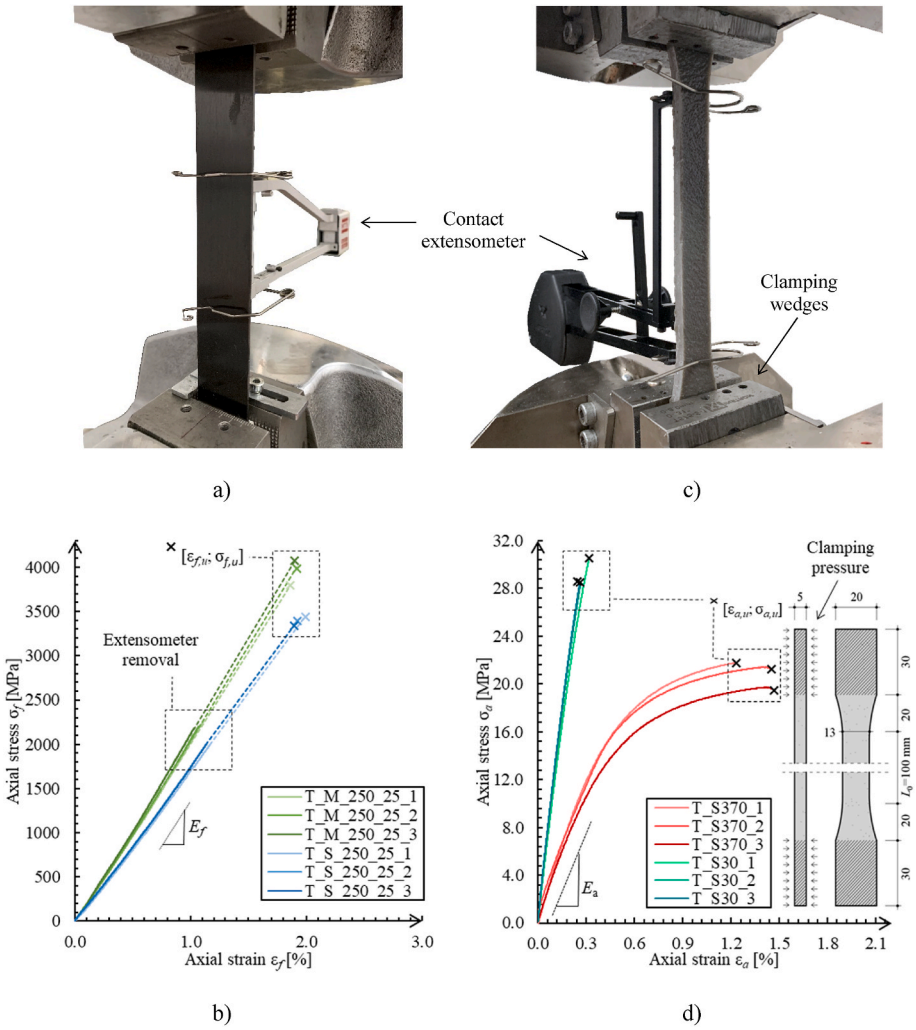

Fig. 1. Photos of test set-up and stress-strain responses of tensile tests: a) and b) CFRP plates and c) and d) adhesives (dimensions in mm).

Table 1
Material properties.

Properties	CFRP		Steel	Adhesive	
	Type M	Type S		Toughened	Brittle
Elastic modulus	E_f = 214 GPa (0.023)	E_f = 176 GPa (0.006)	E_s = 210 GPa$^{\square}$	E_a = 3.65 GPa (0.082)	E_a = 11.54 GPa (0.047)
Yield stress	–	–	σ_y = 275 MPa$^{\square}$	-	-
Tensile strength	$\sigma_{f,u}$ = 3958 MPa (0.035)	$\sigma_{f,u}$ = 3393 MPa (0.014)	$\sigma_{s,u}$ = 430 MPa$^{\square}$	$\sigma_{a,u}$ = 21 MPa (0.052)	$\sigma_{a,u}$ = 29 MPa (0.043)
Ultimate tensile strain	$\varepsilon_{f,u}$ = 1.85 % (0.015)	$\varepsilon_{f,u}$ = 1.93 % (0.013)	$\varepsilon_{s,u}$ = 15 %$^{\square}$	$\varepsilon_{a,u}$ = 1.35 % (0.078)	$\varepsilon_{a,u}$ = 0.28 % (0.115)
Thickness	t_f = 1.4 mm	t_f = 1.4 mm	t_s = 8.0 mm (flange)	t_a = 1.0 mm	t_a = 1.0 mm

Note: $^{\square}$ declared by the manufacturer. CoV values in brackets.

Two epoxy adhesives were considered to bond the CFRP-steel joint. A toughened adhesive, referred to as S370, and a traditional non-toughened adhesive, referred to as S30 [38]. Their mechanical properties were obtained by tensile testing of three dumbbell specimens (Fig. 1c) having the nominal dimensions shown in Fig. 1d, according to ASTM D638-22 [39]. Fig. 1d shows the stress-strain curves of the tested specimens, where the axial strain ε_a was measured using an extensometer with a 100 mm gauge length. The average ultimate tensile stress $\sigma_{a,u}$, the corresponding strain $\varepsilon_{a,u}$, and the elastic modulus E_a, obtained by linear regression of the linear portion of the σ_a - ε_a curve included between $0.15\sigma_{a,u}$ and $0.45\sigma_{a,u}$, are reported in Table 1. According to the classification reported in the literature [7,18,25,26], the adhesive S30 can be classified as a brittle one with high modulus.

Table 1 also reports the mechanical properties of the steel used in the bond tests, as declared by the manufacturer.

4. Experimental set-up

Eighteen single-lap direct shear tests were performed in this experimental campaign according to the dimensions and test set-up shown in Fig. 2. Specimens were realized by bonding the CFRP strip to a flange of a standard HEA 100 steel profile of length 250 mm. The composite bonded area had dimensions $b \times L$ (width × length) and was located 20 mm apart from the support upper edge (see Fig. 2a). The bonded width b = 20 mm was the same for all specimens, whereas three different bonded lengths were considered, namely L = 200 mm, 100 mm, and 70 mm. The substrate was grinded using a steel wire wheel and then cleaned with a solvent. The adhesive thickness was t_a = 1.0 mm. The

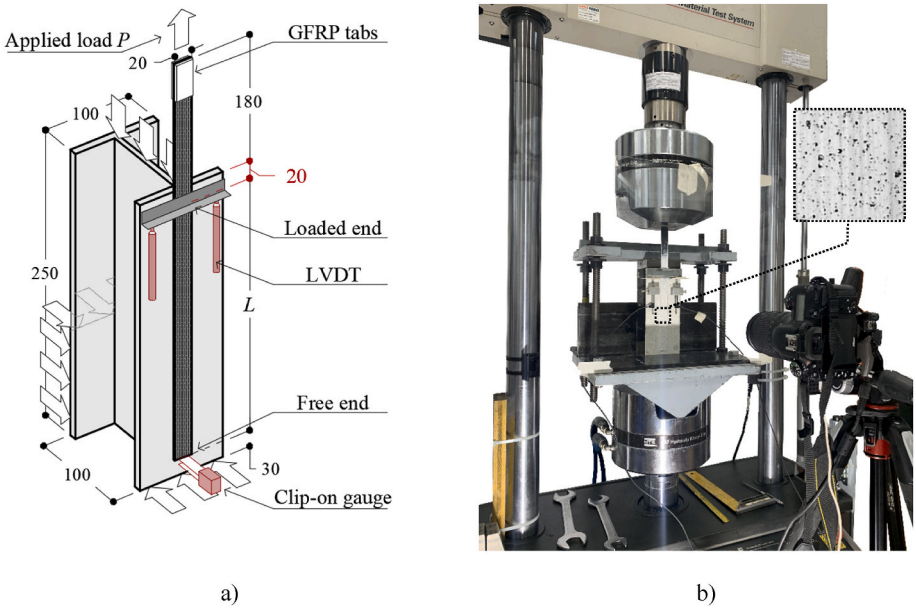

Fig. 2. Single-lap direct shear test set-up: a) sketch (dimensions in mm) and b) photo.

specimens were left to cure for one week in lab conditions before the test. The composite plate extended for 200 mm beyond the upper edge of the bonded area, referred to as the loaded end in Fig. 2a. GFRP tabs were epoxy bonded to the end of the plate to promote a uniform distribution of the testing machine clamping pressure during the test. An L-shaped aluminum plate was bonded to the composite plate at the loaded end and reacted off of two linear variable displacement transformers (LVDT) bonded to the steel substrate on the two sides of the composite strip (see Fig. 2). In three specimens, a clip-on gauge was applied to the specimen free end to track the relative displacement between the FRP plate and the steel substrate at that location (see Fig. 2a).

The specimen was restrained to the testing machine using a steel frame (Fig. 2b). Steel plates were used to prevent the specimen out-of-plane movement. A servo-hydraulic testing machine equipped with a 250 kN load cell was used for the tests. Fifteen tests were conducted in displacement (stroke) control mode at the rate of 0.05 mm/min. For the remaining three specimens, equipped with the clip-on gauge at the free end (see Fig. 2a), the test was initially conducted in displacement control mode, which was then switched to free end clip-on gauge control mode at the rate of 0.005 mm/min.

Before the test, all specimens were painted white and sprayed with black paint to realize a speckle pattern (Fig. 2b). A 21-megapixel camera was used to take pictures of the specimen at a rate of 6 pics per minute throughout the test. A commercial DIC software was used to analyze the images and extract the displacement and strain fields of the specimen strengthened surface.

Specimens were named according to the notation DS(SB)_S370 (or S30)_(S)_*L*_*b*_n, where DS (direct shear) indicates the test set-up, SB, if present, denotes the presence of the clip-on gauge, S370 and S30 identify the toughened and brittle adhesives, respectively, S, if present, indicates that the type S CFRP plate was used (if not indicated, specimens comprise the type M plate), and *L*, *b*, and n are the specimen bonded length (mm), bonded width (mm), and number.

5. Test results

All tested specimens exhibited cohesive debonding within the adhesive layer (Fig. 3). As shown in Fig. 3, the adhesive cohesive failure of specimens with bonded length $L = 200$ mm either developed uniformly close to the FRP side (see specimen DS_S370_200_20_2 in Fig. 3) or

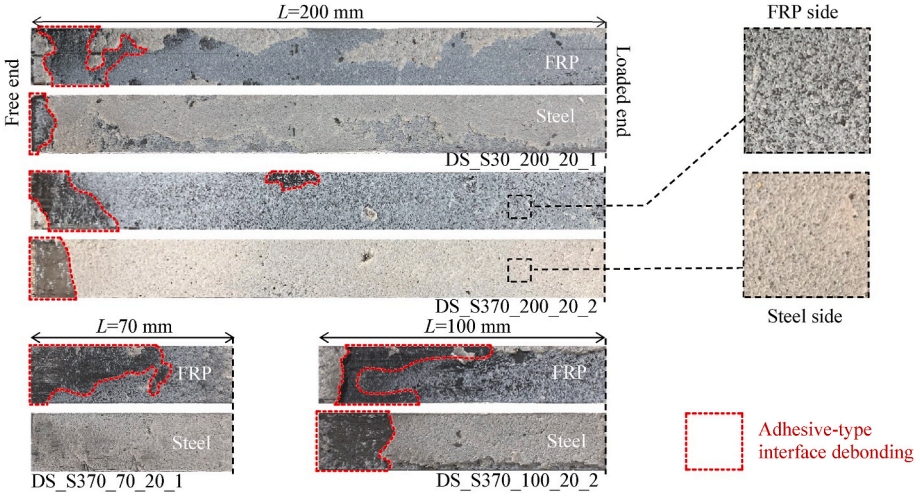

Fig. 3. Failure modes of tested specimens.

propagated within the adhesive with portions close to the FRP side and portions close to the steel side (see specimen DS_S30_200_20_1 in Fig. 3). A similar behavior was observed for the FRP-steel joints presents in Ref. [7], where the cohesive crack started close to the mid-thickness of the adhesive layer and then propagated toward the FRP surface. In all cases, an adhesive-type interface debonding was observed close to the free end, which was attributed to the presence of a Mode-I loading condition in this portion. Fig. 3 shows the joint portion where adhesive-type interface debonding occurred. This was induced by local peeling effects developed at the free end to equilibrate interface shear stress concentrations, which in turn determined the rupture and pull-off of a small adhesive wedge near the free end (Fig. 3). A similar debonding mode was observed in Ref. [7] where the cohesive failure was accompanied by a localized interface failure near the free end, attributed to the presence of high peeling stress. The Mode-I loading can be emphasized in the case of thick FRP plates, where the bending stiffness is high, or high adhesive thickness and can led to brittle adhesive-type failure [7].

For short bonded lengths, namely 100 mm and 70 mm, cohesive debonding always occurred close to the FRP side. However, due to the limited length, the adhesive-type interface debonding at the free end involved a large portion of the bonded length. The joint portion where adhesive-type debonding occurred was 47–53 % of the bonded area for specimens with 70 mm bonded length, whereas it reduced to 25–28 % and 11–14 % for 100 mm and 200 mm bonded length specimens, respectively.

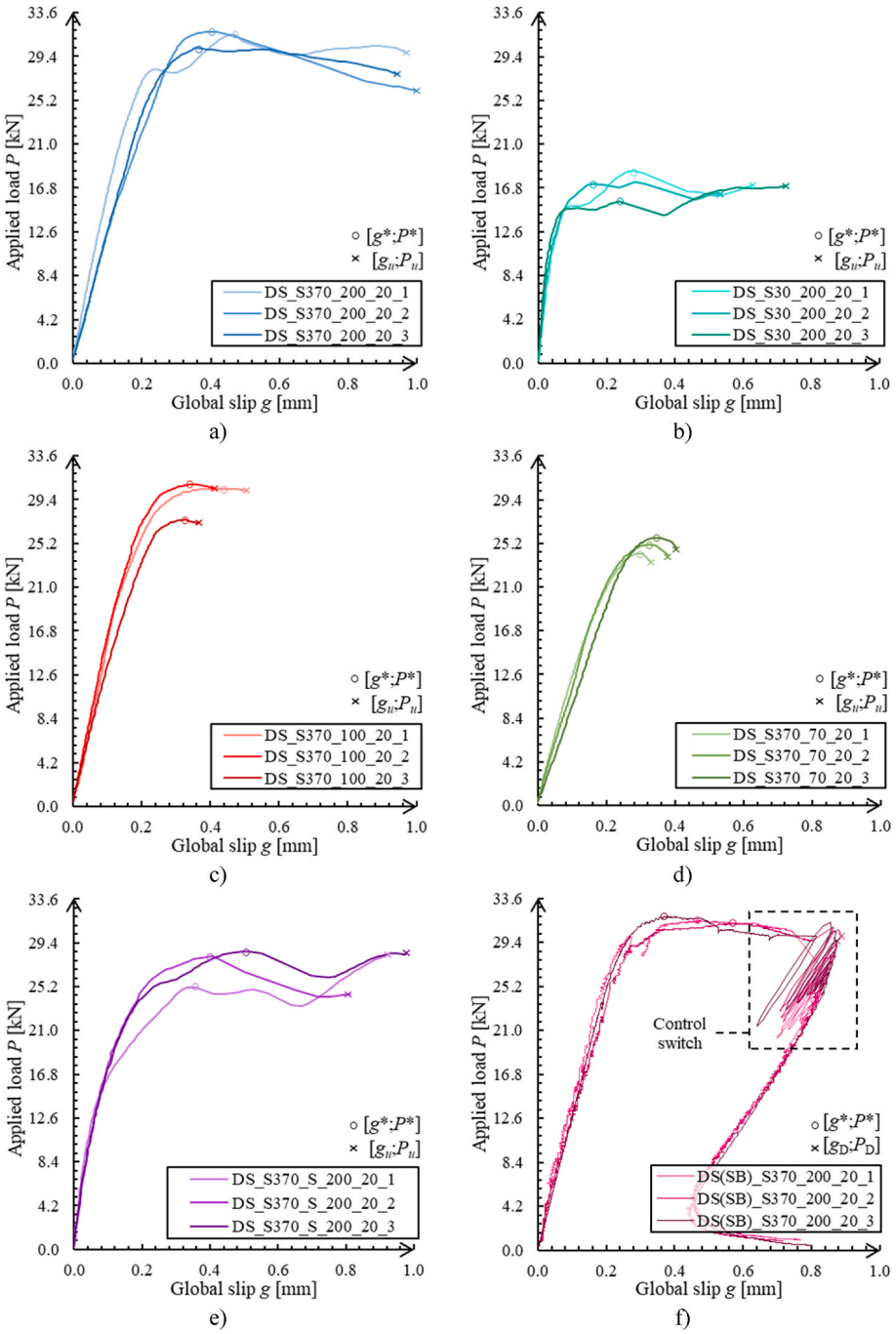

Fig. 4. Experimental applied load – global slip responses: a) specimens DS_S370_200_20_1–3, b) specimens DS_S30_200_20_1–3, c) specimens DS_S370_100_20_1–3, d) specimens DS_S370_70_20_1–3, e) specimens DS_S370_S_200_20_1–3, and f) specimens DS(SB)_S370_200_20_1–3.

5.1. Applied load P – global slip g response

The applied load P – global slip g responses obtained by the direct shear tests are shown in Fig. 4a–f, where g was computed as the average of the two LVDTs readings at the specimen loaded end (Fig. 2). Table 2 reports the key parameters of the P-g responses, alongside with the average values of nominally equal specimens and corresponding coefficients of variation (CoV). Key parameters include the slope of the initial linear branch k_{el}, the peak applied load P^* and the corresponding global slip g^*, the ultimate load (i.e., the load at the specimen failure) P_u and the corresponding global slip g_u, and the global slip associated with the joint ductility $\bar{g}_{duct} = g_u - g^*$ [21]. For specimens DS(SB), the parameters P_u and g_u were replaced by P_D and g_D, associated with the P-g curve point where the maximum global slip was recorded (Fig. 4f). In Table 2, k_{el} was computed by linear regression of points of the P-g curve between $0.2P^*$ and $0.4P^*$, whereas $\bar{g}_{duct} = g_u - g^*$ [or $g_D - g^*$ for DS(SB) specimens] was the difference between the global slip at specimen failure (or at point D for DS(SB) specimens) and that recorded at the peak load.

5.1.1. Specimens tested in displacement control mode

For all specimens tested in displacement control mode until failure (Fig. 4a–e), the P-g curve exhibited an initial linear branch attributed to the elastic behavior of composite and adhesive. Once the adhesive portion closer to the loaded end started undergoing plasticization and microcracking, the load response became non-linear until the peak load P^* was reached. The attainment of the peak load was associated with the onset of debonding at the loaded end. Beyond this point, a constant or slightly decreasing branch associated with the propagation of the cohesive crack and simultaneous shifting of the stress transfer zone from the loaded end toward the free end was observed. For short bonded lengths, the extent of this branch was lower than that exhibited by $L =$ 200 mm specimens. Eventually, a sudden load drop associated with the applied load P_u and global slip g_u was observed, which corresponded with the onset of the adhesive-type interface debonding of the FRP plate near the free end (Fig. 3).

For sufficiently long bonded lengths, cohesive interface models provide a snap-back branch of the P-g curve beyond the end of the constant branch [17,21,40]. The presence of snap-back is due to the elastic strain recovery of the plate while the applied load decreases due to the propagation of debonding. The snap-back branch could not be captured by the displacement-controlled tests, where a maximum reduction of the applied load of 18 % after attaining P^* was observed, with no global slip recovery. The absence of a final descending branch in the experimental load response can be attributed to the test control adopted and to the presence of local peeling effects developed near the joint free end. The constant increasing displacement did not allow the elastic strain recovery of the plate debonded portion, whereas the presence of peeling stress promotes the unstable propagation of interfacial debonding.

5.1.2. Specimens tested in free end slip control mode

To capture the full range cohesive debonding process, specimens DS(SB)_S370_200_20_1–3 were initially tested in displacement control mode, which was then switched to free end clip-on gauge control mode. Fig. 4f shows the P-g curves obtained, which had a shape consistent with that of specimens DS_S370_200_20_1–3 during the quasi-static displacement-controlled stage. Beyond this stage, the clip-on gauge control mode allowed for capturing a descending branch associated with the full propagation of the cohesive crack along the joint. The control switch was manually triggered by the operator at the attainment of a global slip $g = 0.7$ mm. This condition, that applies only to the joints studied, was determined from an analytical model of the joint and represented the global slip beyond which the elastic strain recovery of the plate debonded portion was necessary to allow the complete development of the cohesive debonding process.

When the control switch was triggered, some load oscillations were observed in the P-g curve caused by the testing machine tuning (see Fig. 4f). Beyond this stage, the free end displacement constantly increased and the applied load decreased due to the propagation of the cohesive crack. Simultaneously, snap-back occurred in the P-g curve as a consequence of the load reduction, which allowed the gradual recovery of elastic strain in the CFRP plate debonded portion. In the very last stage of the test, the specimen free end started undergoing some out of plane displacement due to the presence of local peeling stress. This made the clip-on gauge reading (and so the test control mode) no longer reliable.

Table 2
Key parameters of the experimental P-g responses.

Specimen	k_{el} [kN/mm]	P^* [kN]	g^* [mm]	Pu (or P_D) [kN]	gu (or g_D) [mm]	$\bar{g}_{duct}$ [mm]
DS_S370_200_20_1	161	31.51	0.46	29.82	0.97	0.50
DS_S370_200_20_2	122	31.77	0.40	26.12	0.99	0.59
DS_S370_200_20_3	128	30.22	0.36	27.78	0.94	0.58
Average	137	31.17	0.41	27.91	0.97	0.56
CoV	0.151	0.027	0.125	0.066	0.029	0.083
DS(SB)_S370_200_20_1	122	31.47	0.47	27.90	0.85	0.38
DS(SB)_S370_200_20_2	128	31.22	0.57	29.99	0.89	0.31
DS(SB)_S370_200_20_3	128	31.88	0.37	29.52	0.87	0.50
Average	126	31.52	0.47	29.14	0.87	0.40
CoV	0.029	0.011	0.214	0.038	0.019	0.235
DS_S370_100_20_1	159	30.44	0.44	30.31	0.50	0.06
DS_S370_100_20_2	160	30.85	0.34	30.45	0.41	0.07
DS_S370_100_20_3	130	27.47	0.33	27.13	0.37	0.04
Average	150	29.59	0.37	29.30	0.43	0.06
CoV	0.117	0.062	0.172	0.064	0.157	0.291
DS_S370_70_20_1	120	24.20	0.31	23.51	0.33	0.02
DS_S370_70_20_2	102	25.11	0.32	24.08	0.38	0.06
DS_S370_70_20_3	97	25.74	0.33	24.78	0.40	0.07
Average	106	25.02	0.32	24.12	0.37	0.05
CoV	0.112	0.031	0.041	0.026	0.105	0.521
DS_S30_200_20_1	310	18.44	0.28	17.03	0.62	0.35
DS_S30_200_20_2	362	17.35	0.28	16.26	0.53	0.25
DS_S30_200_20_3	397	15.50	0.24	17.05	0.72	0.49
Average	357	17.10	0.27	16.78	0.63	0.30
CoV	0.124	0.087	0.096	0.027	0.153	0.237
DS_S370_S_200_20_1	201	25.15	0.33	28.18	0.92	0.59
DS_S370_S_200_20_2	181	28.14	0.41	24.52	0.81	0.40
DS_S370_S_200_20_3	175	28.57	0.52	28.35	0.98	0.46
Average	186	27.29	0.4	27.02	0.90	0.43
CoV	0.075	0.068	0.222	0.080	0.093	0.091

Note: For specimens type DS(SB), the sixth and the fifth columns indicate the maximum global slip g_D and the corresponding applied load P_D, respectively.

6. Interfacial stress-strain distribution

A pure Mode-II loading condition is usually assumed in single-lap DS test [7,40–43]. Accordingly, the bond behavior of adhesively bonded FRP-steel joints exhibiting a cohesive failure within the adhesive layer can be described by a CML that relates the shear stress in the adhesive layer τ with the slip between the FRP and steel substrate s.

In single-lap DS tests of FRP-substrate joints, the $\tau(s)$ law can be obtained experimentally by directly measuring the axial strain $\varepsilon(x)$ along the applied load direction x (direct method) using contact (e.g., strain gauges [7]) and non-contact techniques (e.g., DIC [44]). The interface shear stress $\tau(x)$ and slip $s(x)$ are then obtained through derivation and integration of $\varepsilon(x)$, respectively, which allows for obtaining

the parametric expression of the $\tau(s)$ law [21,45]:

$$\begin{cases} \tau(\bar{x}) = \dfrac{E_f A_f}{b} \left.\dfrac{d\varepsilon(x)}{dx}\right|_{x=\bar{x}} \\ s(\bar{x}) = \displaystyle\int_0^{\bar{x}} \varepsilon\,(x)dx \end{cases} \quad \text{for } 0 \le \bar{x} \le L \tag{1}$$

where the parameter $\bar{x}$ is a coordinate along the bonded length L. Note that Eq. (1) was obtained assuming rigid substrate and a pure Mode-II loading condition.

Alternatively, $\tau(s)$ curves can be determined by indirect methods that consider the $P(g)$ response of direct shear tests. For instance, the approach proposed by Zhu et al. [45] provides the $\tau(s)$ imposing the equilibrium of an infinitesimal portion of the matrix-fiber interface under the assumptions of rigid substrate and pure Mode-II loading condition:

$$\tau(s) = \left.\frac{dP}{dg}\right|_{g=s} \frac{P}{E_f A_f b} \tag{2}$$

In this paper, the $\tau(s)$ was obtained by the direct method using the DIC technique. Fig. 5a and b show the $\varepsilon(x)$ axial strain profiles for specimens DS_S370_200_20_1 and DS_S30_200_20_2, measured at different global slip g values. The strains were obtained using the DIC on an area approximately 2 mm-wide at the center of the CFRP plate, considering a subset and step with edge of 21 pixel (approximately 1.22 mm) and 5 pixel (approximately 0.29 mm), respectively. As shown in Fig. 5a and b, a certain scatter was observed in the experimental strain recorded by the DIC, which is particularly relevant along the strip debonded portion. This can be attributed to the irregularity of the cohesive crack surface, which could result in stress concentrations. In Fig. 5a and b, a representative strain profile corresponding to $g = 0.5$ mm for specimen DS_S370_200_20_1 and to $g = 0.3$ mm for specimen DS_S30_200_20_2 was smoothed to reduce the measurement noise. Smoothing was done using the Local Regression Method function named *smooth* of Matlab®. The process is local because each smoothed value is determined from all the data points inside a given interval, as for the moving average method. The process is also weighted since a weight function is introduced for the data points inside the selected interval. This allows to reduce the effect of outliers on the smoothed values which are then consistent with most of the data points.

The smoothed S-shaped $\varepsilon(x)$ profiles shown in Fig. 5a and b can be divided into three main zones, namely the stress-free zone (SFZ), stress transfer zone (STZ) and debonded zone (DZ). In the SFZ, the axial strain can be considered zero and the adhesive not engaged in the bond stress transfer. The STZ represents the portion of the interface where the stress transfer mechanism takes place. In this zone, the adhesive portion closer to the free end is in the elastic phase whereas the remaining part entered the non-linear phase. The length of the STZ, i.e., the minimum distance between the first point where $\varepsilon(x)$ is equal to zero and the point where the derivative $d\varepsilon(x)/dx$ reaches zero, is referred to as the effective bond length l_{eff}, or the minimum length needed to fully establish the composite-substrate bond stress transfer mechanism. In the DZ, the reinforcement is debonded from the substrate and the axial strain is constant. As shown in Fig. 5a and b, comparing axial strain profiles corresponding to different global slip g values, a shift of the STZ toward the free end can be observed, which entails for an increase of the DZ.

Fig. 5c and d show the experimental τ-s curves of specimens DS_S370_200_20 and DS_S30_200_20, respectively, obtained from the

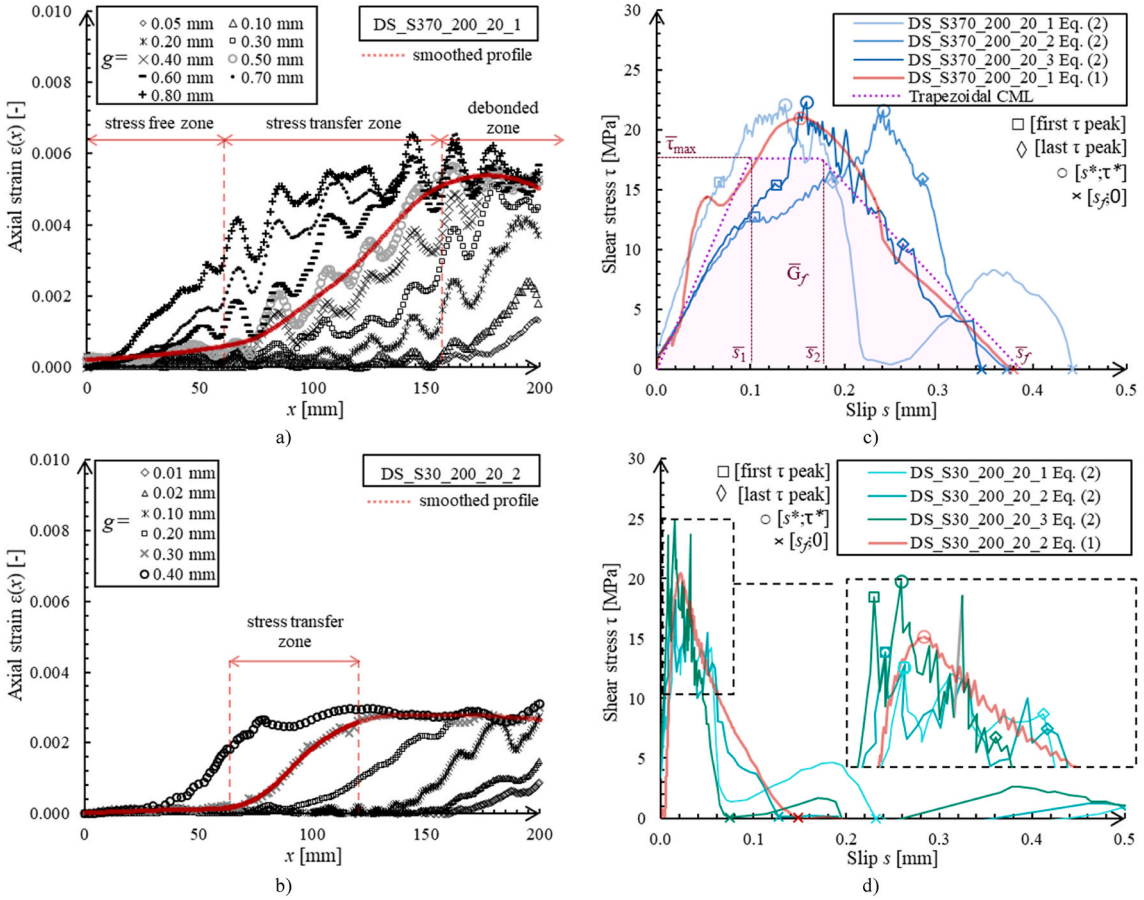

Fig. 5. Axial strain distribution along the bonded length at different values of global slip: a) specimen DS_S370_200_20_1 and b) specimen DS_S30_200_20_2. $\tau(s)$ curves of specimens c) DS_S370_200_20_1–3 and d) DS_S30_200_20_1–3.

corresponding *P-g* responses (see Fig. 4a and b) using Eq. (2). Fig. 5c and d also show the τ-*s* curves of specimens DS_S370_200_20_1 and DS_S30_200_20_2, respectively, obtained applying Eq. (1) to the corresponding smoothed ε(*x*) profiles reported in Fig. 5a and b. For all specimens considered, the τ-*s* curve had an initial ascending branch associated with the adhesive elastic behavior. Following the ascending branch, the τ-*s* curve of specimens with the toughened adhesive showed a sub-horizontal or slightly ascending branch attributed to the adhesive ductility, whereas for specimens with the brittle adhesive this branch was not visible. The maximum shear stress associated with the τ-*s* curve, i.e., the interface bond strength, is referred to as τ^* and the corresponding slip as s^*. In its final stage, the τ-*s* curve was characterized by a descending branch attributed to the adhesive softening. Eventually, when the cohesive crack was fully developed and the reinforcement debonded, the shear stress reduced to $\tau = 0$, which is associated with the slip s_f. For each τ-*s* curve, the parameters τ^*, s^*, and s_f are marked in Fig. 5c and d. The area below the τ-*s* curve is the fracture energy G_f.

The τ-s curves obtained from DIC analysis and Eq. (1) showed good agreement with those obtained using Eq. (2) (see also Table 3). Differences of 5–6 % and 4–10 % were recorded on τ^* and G_f, respectively. Besides, τ-s curves obtained by Eq. (1) were generally smoother than those obtained by Eq. (2). This can be attributed to the quality (continuity) of the ε(*x*) profile obtained through DIC analysis and to the smoothing. Conversely, load oscillations in the *P-g*, which were not smoothed, determined oscillation in the d*P*/d*g*, which in turn determined a certain scatter in the τ-s curves obtained by Eq. (2).

7. Analysis and discussion of experimental results

In this section, the results of direct shear tests are analyzed and discussed. The effect of different bonded lengths, adhesive types, and composite elastic moduli and the influence of slip reading technique are considered. The experimental results are also compared with the analytical predictions of a cohesive interface model for FRP-steel joints with toughened adhesives previously presented by the authors [21]. This model considers a multi-linear trapezoidal CML that comprises an elastic ascending branch, an horizontal plastic branch, and a final descending softening branch. The presence of a plastic phase in the adopted CML allowed for capturing the sub-horizontal or slightly ascending branch observed in the shear stress distribution of Fig. 5c. Furthermore, the analytical model allowed for describing the load response snap-back captured experimentally.

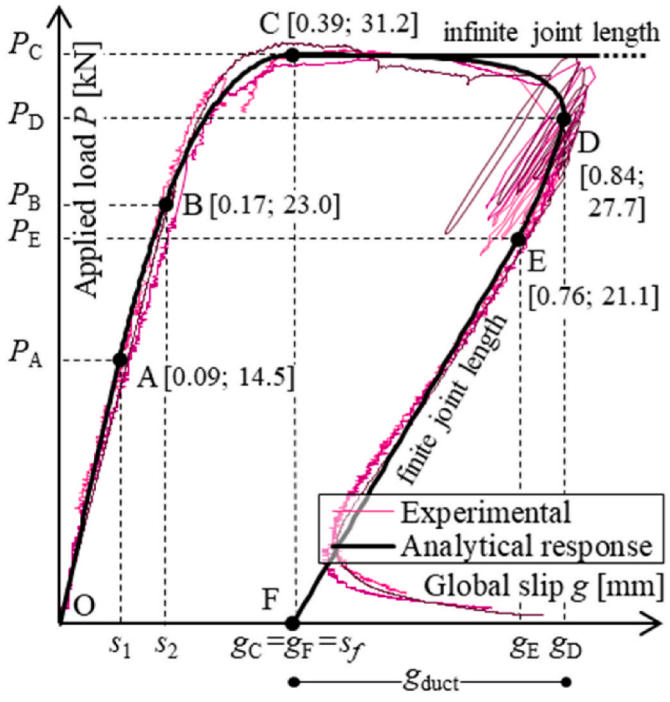

Fig. 6. Comparison between analytical and experimental *P-g* responses for specimens DS(SB)_S370_200_20_1–3 (stages of the debonding process are also indicated).

7.1. Analytical model

Under a pure Mode-II loading condition, the equilibrium of an infinitesimal segment of composite of length d*x* provides the bond differential equation (Eq. (a) in Table 4). For a bonded length *L* higher than the effective bond length l_{eff} and provided the trapezoidal CML of Eq. (3), Eq. (a) can be solved to obtain the analytical shear stress τ(*x*) distributions associated with six subsequent stages that fully describe the debonding process of a steel-FRP joint exhibiting cohesive failure within the adhesive.

$$\tau(s) = \begin{cases} k_1 s & 0 \le s \le s_1 \\ \tau_{max} & s_1 < s \le s_2 \\ -k_2(s - s_f) & s_2 < s \le s_f \\ 0 & s > s_f \end{cases} \tag{3}$$

In Eq. (3), τ_{max} is the interface bond strength, s_1 and s_2 are the slip at the end of the elastic and plastic phases, respectively, s_f is the slip at the onset of debonding, and k_1 and $-k_2$ are the slope of the linear elastic and linear softening branches, respectively. Table 4 reports the shear stress τ(*x*) distribution corresponding to the following six stages of the debonding process:

1. Elastic stage: the entire adhesive length is in the elastic phase. This stage ends once the maximum shear stress τ_{max} is attained at the loaded end.
2. Elastic-plastic stage: the plastic phase is engaged along a length a_t, while along the segment $L - a_t = t$ the interface is in the elastic phase.
3. Elastic-plastic-softening stage: the interface length l_t close to the loaded end entered the softening phase. Along the remaining portion the interface is in the plastic phase along the length a_t and in the elastic phase along the length *t*. This stage ends when the shear stress at the loaded end reduces to 0 and the bond stress-transfer mechanism is fully established.
4. Elastic-plastic-softening-debonding stage: in this stage, the interface portion of length d_t close to the loaded end is fully debonded, while the stress-transfer zone translates toward the free end (i.e., $x = 0$). This stage ends when the shear stress $\tau(0) = \tau_{max}$ is attained at the joint free end.
5. Plastic-softening-debonding stage: in this stage, the interface is in the plastic phase along the length *a*, whereas the portion associated with the softening phase with length l_a moves toward the free end. In this stage, the length of the interface debonded portion, referred to as d_a in Table 4, increases with the reduction of *a*. This stage ends when the interface portion engaged in the plastic phase reduces to zero.
6. Softening-debonding stage: during this stage, the interface portion subjected to the softening phase has a length constantly equal to l_{sb}, whereas the shear stress at the free end τ(0) reduces from τ_{max} to zero. At the end of this stage the plate is fully debonded.

7.2. Calibration of the CML and analytical load response

In [21], the authors proposed a calibration procedure to obtain the five parameters of the trapezoidal CML, namely τ_{max}, s_1, s_2, s_f, and G_f, which can be identified on the experimental τ-*s* curve (see Fig. 5c). Only four parameters were considered as independent variables in the calibration procedure (τ_{max}, s_1, s_f, and G_f), while one (s_2) was obtained as a function of the other four. According to the procedure proposed: the fracture energy G_f was defined as the area below the curve until $\tau = 0$;

Table 3
Significant parameters of the τ-*s* responses.

Specimen	τ* [MPa]	*s** [mm]	s_f [mm]	G_f [N/mm]	τ_{max} [MPa]	s_1 [mm]	s_2 [mm]
DS_S370_200_20_1 Eq. (2)	22.1	0.136	0.442	4.198	19.2	0.066	0.066
DS_S370_200_20_2 Eq. (2)	21.6	0.241	0.372	4.168	16.7	0.104	0.233
DS_S370_200_20_3 Eq. (2)	22.4	0.159	0.346	3.787	17.0	0.128	0.227
Average: Trapezoidal CML	–	–	0.387	4.051	17.6	0.099	0.175
DS_S370_200_20_1 Eq. (1)	21.0	0.152	0.379	4.377	–	–	–
DS_S30_200_20_1 Eq. (2)	18.0	0.016	0.232	1.268	14.5	0.016	0.115
DS_S30_200_20_2 Eq. (2)	19.2	0.010	0.127	1.079	14.2	0.010	0.035
DS_S30_200_20_3 Eq. (2)	24.9	0.015	0.075	0.921	17.5	0.007	0.038
DS_S30_200_20_2 Eq. (1)	20.4	0.021	0.149	1.195	–	–	–

Table 4
Interfacial shear stress distribution along the bonded joint for each stage of the debonding process and corresponding *P*-*g* equations. See Fig. 6 for the representation of the loading stages.

Stage	*P*–*g* equations	τ(*x*) distributions
Bond differential equation	$\frac{d^2 s}{dx^2} - \frac{b}{E_f A_f}\tau(s) = 0$ (a)	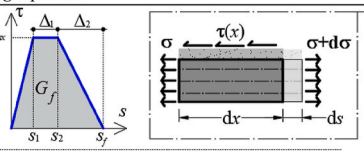
Elastic	$P = \left[E_f A_f \lambda \tanh(\lambda L)\right] g \quad 0 \le g \le s_1$ (b)	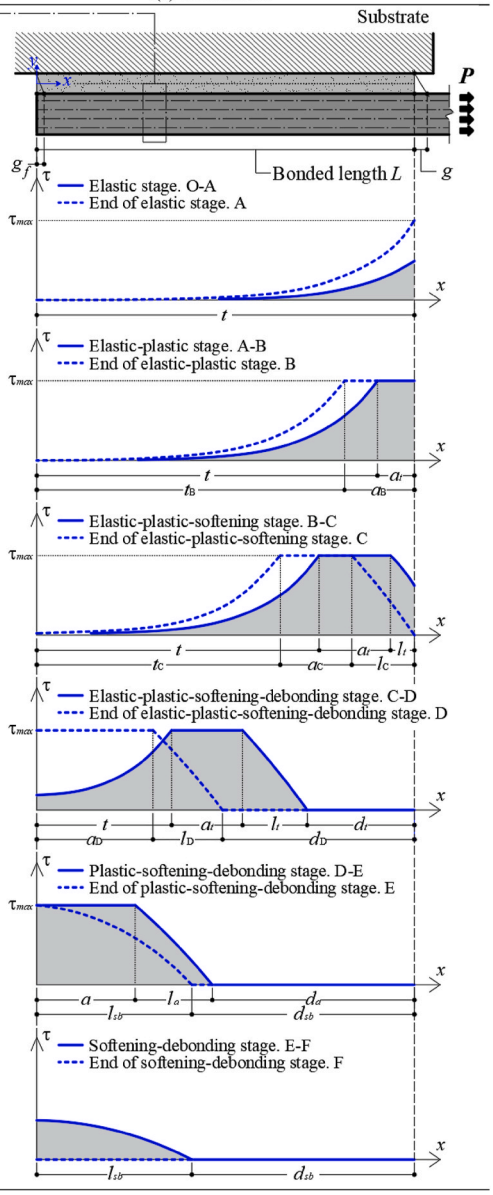
End of stage	$\begin{cases} P_A = E_f A_f \lambda s_1 \tanh(\lambda L) \\ g_A = s_1 \end{cases}$ (c)	
Elastic-plastic	$\begin{cases} P = E_f A_f \lambda s_1 \left[\lambda a_t + \tanh(\lambda t)\right] \\ g = \frac{\lambda^2 s_1}{2} a_t^2 + \lambda s_1 \tanh(\lambda t) a_t + s_1 \end{cases} \quad t_B \le t \le L$ (d)	
End of stage	$\begin{cases} P_B = E_f A_f \lambda s_1 \left[\lambda a_B + \tanh(\lambda t_B)\right] \\ g_B = s_2 \end{cases}$ (e)	
Elastic-plastic-softening	$\begin{cases} P = E_f A_f \left\{\omega^2 \Delta_2 \left[a_t + \frac{1}{\lambda}\tanh(\lambda t)\right]\cos(\omega l_t) + \omega \Delta_2 \sin(\omega l_t)\right\} \\ g = \omega \Delta_2 \left[a_t + \frac{1}{\lambda}\tanh(\lambda t)\right]\sin(\omega l_t) - \Delta_2 \cos(\omega l_t) + s_f \end{cases} \quad t_C \le t \le t_B$ (f)	
End of stage	$\begin{cases} P_C = \frac{b\tau_{max}}{\omega}\sqrt{1 + \frac{\omega^2}{\lambda^2}\left[\tanh^2(\lambda t_C) + \frac{2\Delta_1}{s_1}\right]} \\ g_C = s_f \end{cases}$ (g)	
Elastic-plastic-softening-debonding	$\begin{cases} P = E_f A_f \omega \Delta_2 \left\{\omega\left[a_t + \frac{1}{\lambda}\tanh(\lambda t)\right]\cos(\omega l_t) + \sin(\omega l_t)\right\} \\ g = \omega \Delta_2 \left\{\omega\left[a_t + \frac{1}{\lambda}\tanh(\lambda t)\right]\cos(\omega l_t) + \sin(\omega l_t)\right\} d_t + s_f \end{cases} \quad 0 \le t \le t_C$ (h)	
End of stage	$\begin{cases} P_D = E_f A_f \omega \Delta_2 \left[\omega a_D \cos(\omega l_D) + \sin(\omega l_D)\right] \\ g_D = \left[\omega^2 \Delta_2 a_D \cos(\omega l_D) + \omega \Delta_2 \sin(\omega l_D)\right] d_D + s_f \end{cases}$ (i)	
Plastic-softening-debonding	$\begin{cases} P = E_f A_f \omega \Delta_2 \left[\omega a \cos(\omega l_a) + \sin(\omega l_a)\right] \\ g = \omega \Delta_2 \left[\omega a \cos(\omega l_a) + \sin(\omega l_a)\right] d_a + s_f \end{cases} \quad 0 \le a \le a_D$ (l)	
End of stage	$\begin{cases} P_E = E_f A_f \omega \Delta_2 \\ g_E = \omega \Delta_2 d_{sb} + s_f \end{cases}$ (m)	
Softening-debonding	$\begin{cases} P = E_f A_f \omega \left(s_f - g_f\right) \\ g = \omega \left(s_f - g_f\right) d_{sb} + s_f \end{cases} \quad s_2 \le g_f \le s_f$ (n)	
End of stage	$\begin{cases} P_F = 0 \\ g_F = s_f \end{cases}$ (o)	

Note: $\lambda^2 = \frac{bk_1}{E_f A_f}$; $\omega^2 = \frac{bk_2}{E_f A_f} = \lambda^2 \frac{s_1}{\Delta_2}$.

τ_{max} was considered as the average of τ values included between the first and last τ peak, where a peak was defined as the point before which a drop of shear stress of at least 5 % occurred (see Fig. 5c); s_1 was the slip associated with the first τ peak; and s_f was the slip associated with the first $\tau = 0$ point. Finally, s_2 was the slip associated with the last τ peak. The CML parameters estimated from the experimental τ-s curves of specimens DS_S370_200_20 are marked in Fig. 5c and reported in Table 3 along with their average values (indicated with an overbar in Fig. 5c).

Provided a calibration of the trapezoidal CML parameters and adopting the proper boundary conditions, Eq. (a) can be solved to obtain the six branches of the analytical *P-g* curve represented in Fig. 6, namely O-A, A-B, B–C, C-D, D-E, and E-F, whose solution is reported in Table 4. The first linear branch O-A of the *P-g* curve is due to the elastic behavior of composite and interface. After point A, which coincides with the end of the elastic stage (see Table 4), the elastic-plastic stage begins (segment A-B in Fig. 6) and the *P-g* curve becomes non-linear due to the plasticization of the portion of adhesive close to the loaded end. Beyond point B, the joint enters the elastic-plastic-softening stage, and the *P-g* curve is represented by the segment B–C (see Fig. 6). The softening propagation in the adhesive determines a progressive decrease of the *P-g* curve slope, which eventually leads to the attainment of point C, representing the end of this stage. Table 4 shows the shear stress distribution along the bonded length associated with the attainment of point C, where a portion of adhesive of length l_C close to the loaded end is engaged in the softening phase, an intermediate portion of length a_C is in the adhesive plastic phase, and the remaining portion of length t_C is in the elastic phase. The lengths l_C, a_C, and t_C depends both on the CML parameters and on the joint mechanical and geometrical properties and can be numerically obtained using Eq. (4), Eq. (5), and Eq. (6).

$$a_C = \frac{1}{\lambda}\left[\sqrt{\tanh^2(\lambda t_C) + \frac{2\Delta_1}{s_1}} - \tanh(\lambda t_C)\right] \tag{4}$$

$$l_C = \frac{1}{\omega}\arctan\left\{\frac{\lambda}{\omega[\lambda a_C + \tanh(\lambda t_C)]}\right\} \tag{5}$$

$$t_C = L - l_C - a_C \tag{6}$$

If an infinite bonded length is considered, the joint bond capacity P_{max} is attained at the end of the elastic-plastic-softening stage (P_C=P_{max}) and its value can be obtained from Eq. (g) in Table 4 by assuming $\tanh(\lambda t_C) = 1$:

$$P_{max} = \frac{b\tau_{max}}{\omega}\sqrt{1 + \frac{\omega^2}{\lambda^2}\left(1 + \frac{2\Delta_1}{s_1}\right)} = \sqrt{2E_f A_f b G_f} \tag{7}$$

Further increases of the global slip beyond point C results in the opening and propagation of a cohesive crack in the portion of adhesive close to the loaded end while the stress transfer zone (STZ) moves toward the free end. If an infinite bonded length is assumed, the shifting of the STZ is associated with a load plateau at the value P_{max} in the *P-g* curve (see Fig. 6). For finite joint lengths, the cohesive crack propagation results in a gradual decrease of the adhesive portion engaged in the elastic phase, which in turn determines a reduction in the applied load *P* along the branch C-D. When the interface elastic portion is no longer present, point D is reached and the plastic-softening-debonding stage begins. In this stage, the *P-g* curve describes the branch D-E, which is characterized by a further decrease of applied load due to the propagation of the cohesive crack and the corresponding reduction of the length engaged in the plastic phase *a* (see Table 4). In this branch, the global slip reduces due to the elastic strain recovery along the debonded portion resulting from the decrease of the applied load. This phenomenon, called snap-back [46,47], can be observed only for bonded lengths higher than a certain length l_{sb}, referred to as the snap-back length in Refs. [21,48]. At the end of the plastic-softening-debonding stage, point E is reached and no portion of the interface is in the plastic phase. Thus, from this point the interface is in the softening and debonding phases only. Beyond point E, the adhesive softening determines a further reduction of *P*, represented by segment E-F in Fig. 6. Eventually, the strip fully debonds when point F is reached.

Fig. 6 shows a comparison between the analytical load response and the experimental *P-g* curves of specimens DS(SB)_S370_200_20_1–3. An analogous comparison with the experimental responses of specimens DS_S370_200_20_1–3, DS_S370_100_20_1–3, and DS_S370_70_20_1–3 was presented in Ref. [21], whereas different calibrations are required to reproduce the response of specimens with S30 resin. In this study, specimens DS(SB)_S370 were considered for comparison because the test control mode allowed for capturing the snap-back phenomenon (i.e., branches D-E and E-F). Good agreement was found between experimental and analytical results, both in the ascending and post-peak descending branches, except for the final part of the load response. The difference between analytical and experimental results in this portion was attributed to the presence of out-of-plane displacements of the strip, which affected the global slip measure. A 0.9 % and 17.7 % difference was obtained between P_C and the average peak load $\overline{P}^* = 31.53$ kN (Table 2) and between g_C and the average global slip associated with the peak load $\overline{g}^* = 0.47$ mm (Table 2), respectively. Similarly, a 4.9 % and 3.9 % difference was observed between P_D and the average ultimate load $\overline{P}_D = 29.14$ kN (Table 2) and between g_D and the average global slip associated with the ultimate load $\overline{g}_D = 0.87$ mm (Table 2), respectively. Finally, the average experimental $\overline{k}_{el} = 137$ kN/mm was 13.5 % lower than the analytical prevision.

7.3. Remarks on the specimen bonded length

Fig. 4a, c, and d show the load responses of the CFRP-steel joints with toughened adhesive and bonded lengths $L = 200$ mm, $L = 100$ mm, and $L = 70$ mm. The average peak load attained by the short bonded lengths was 5 % ($L = 100$ mm) and 20 % ($L = 70$ mm) lower than that of the series with $L = 200$ mm (see Table 2). Similarly, a 10 % and 22 % lower $\overline{g}^*$ was obtained for $L = 100$ mm and $L = 70$ mm, respectively, compared with that of $L = 200$ mm. The average slope of the *P-g* response initial ascending branch $\overline{k}_{el}$ of specimens with $L = 200$ mm and 100 mm was similar, whereas it was approximately 22 % lower for $L = 70$ mm specimens. The relationship between the joint peak load and bonded length observed was confirmed by the analytical previsions presented in Ref. [21] and summarized in Table 4, which also described the reduction of k_{el} with reducing the bonded length. According to the analytical model, when a bonded length higher than or equal to the effective bond length l_{eff} is provided, the bond-transfer mechanism can be fully established and the joint bond capacity can be attained.

However, a finite value of l_{eff} cannot be defined due to the cosine-hyperbolic shape of the $\tau(x)$ distribution in the elastic phase, which tends asymptotically to $\tau = 0$ and does not allow for identifying the end of the STZ. l_{eff} can then be estimated as the bonded length associated with a certain percentage of P_{max} by considering the parameter α [see Eq. (g) in Table 4 and Eq. (7)] [41,49]:

$$\alpha = \frac{P_C}{P_{max}} = \frac{\xi}{\omega \sin(\omega l_C)} \tag{8}$$

where

$$\xi = \frac{\omega}{\sqrt{1 + \frac{\omega^2}{\lambda^2}\left(1 + \frac{2\Delta_1}{s_1}\right)}} \tag{9}$$

Thus, $l_{eff}(\alpha)$ can be defined as:

$$l_{eff}(\alpha) = t_C(\alpha) + a_C(\alpha) + l_C(\alpha) \tag{10}$$

where $t_C(\alpha)$, $a_C(\alpha)$, and $l_C(\alpha)$ were determined by introducing Eq. (8) into Eq. (4), Eq. (5), and Eq. (6):

$$t_C(\alpha) = \frac{1}{\lambda}\tanh^{-1}\left[\sqrt{\frac{\lambda^2\alpha^2}{\xi^2}\left(1-\frac{\xi^2}{\omega^2\alpha^2}\right)-\frac{2\Delta_1}{s_1}}\right] \quad (11)$$

$$a_C(\alpha) = \frac{\alpha}{\xi}\sqrt{1-\frac{\xi^2}{\omega^2\alpha^2}} - \frac{1}{\lambda}\sqrt{\frac{\lambda^2\alpha^2}{\xi^2}\left(1-\frac{\xi^2}{\omega^2\alpha^2}\right)-\frac{2\Delta_1}{s_1}} \quad (12)$$

$$l_C(\alpha) = \frac{1}{\omega}\arcsin\left(\frac{\xi}{\omega\alpha}\right) \quad (13)$$

Fig. 7a shows the function $l_{eff}(\alpha)$ for the calibrated trapezoidal CML in Fig. 5c and Table 3 and indicates that a bonded length of 133 mm would be sufficient to develop the 98 % of P_{max}. As expected, the parameter α mostly affects the interface length engaged in the elastic phase t_C (Fig. 7b), whereas a_C and l_C do not vary significantly with α. Eqs. (11)–(13) show that $l_{eff}(\alpha)$ depends both on the mechanical and geometrical properties of the FRP reinforcement (i.e., E_f, A_f, and b) and on the CML parameters, which are affected by the adhesive type.

Increasing the bonded length beyond the effective bond length, the specimen peak load remains approximately constant and equal to the bond capacity, while the global slip at failure, g_u, and slip ductility (i.e., g_{duct}, see Section 5.1) increase. The experimental results confirmed this behavior, with specimens of series DS_S370_200_20 providing an average slip at failure $\overline{g}_u$ 127 % and 162 % higher than that of specimens with $L = 100$ mm and $L = 70$ mm, respectively. Similarly, the average slip ductility of specimens DS_S370_100_20 ($\overline{g}_{duct} = 0.06$ mm) and DS_S370_100_20 ($\overline{g}_{duct} = 0.05$ mm) were 11 % and 9 % of that of specimens with $L = 200$ mm ($\overline{g}_{duct} = 0.56$ mm, see Table 2). Accordingly, results of CFRP-steel joints with a different toughened adhesive and $L = 300$ mm and $L = 380$ mm presented in Ref. [7] showed ultimate global slips in the range $g_u = [2.00, 2.70]$ mm with high slip ductility. This confirmed that high bonded lengths entail for high displacement capacity of the joint.

7.4. Effect of adhesive type

Fig. 4a and b show the P-g responses of specimens with toughened (series DS_S370) and traditional (series DS_S30) adhesives, respectively. Despite the same bonded length considered ($L = 200$ mm) and cohesive failure mode obtained (Fig. 3), specimens of series DS_S370 showed a 82 % and 66 % higher average bond capacity ($\overline{P}^*$) and ultimate load ($\overline{P}_u$), respectively, than those of specimens DS_S30. Similarly, the average peak global slip ($\overline{g}^*$), ultimate global slip ($\overline{g}_u$), and slip ductility ($\overline{g}_{duct}$) were 53 %, 54 %, and 87 % higher for specimens with the toughened adhesive than with the traditional adhesive. This behavior was attributed to the higher fracture toughness and strain capacity ($\varepsilon_{a,u}$, see Table 1) of the toughened adhesive than of the traditional adhesive, which in turn resulted in a 272 % higher average fracture energy $\overline{G}_f$ (see Table 3). However, the traditional adhesive was associated with a 160 % higher average slope of the initial linear branch ($\overline{k}_{el}$) of the P-g curve for specimens of series DS_S30, if compared with that for specimens of series DS_S370 (Table 2). This was attributed to the higher stiffness and lower strain capacity of traditional adhesives with respect to those of toughened adhesives.

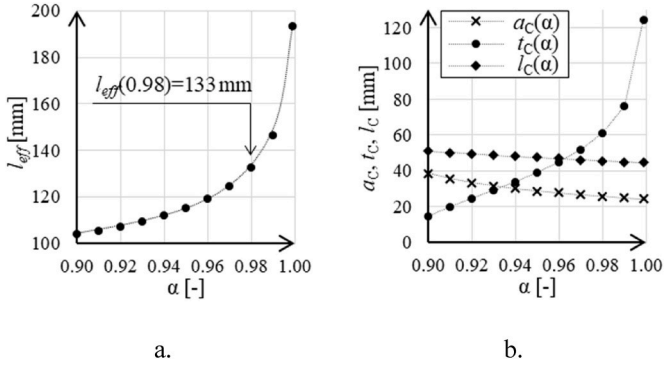

Fig. 7. Variation of l_{eff} (a) and t_C, a_C, and l_C (b) with α.

The higher bond capacity provided by joints with toughened adhesive was confirmed by Eq. (7), where P_{max} is expressed as a nonlinear function of G_f. The high toughness of the S370 adhesive also affected the shape of the $\varepsilon(x)$ axial strain distribution along the bonded length. As shown in Fig. 5a and b, specimen DS_S370_200_20_1 provided a wider amplitude of the STZ with respect to that of specimen DS_S30_200_20_2. This indicated that a higher bonded length was needed to fully establish the bond stress transfer mechanism when using toughened rather than traditional adhesives. Besides, the different shapes of the shear stress - slip relationships associated with the toughened (Fig. 5c) and traditional (Fig. 5d) adhesives entailed for different axial strain $\varepsilon(x)$ behaviors along the bonded length (see Fig. 5a and b). Indeed, according to the analytical model, the presence of the plateau in the trapezoidal CML determined an almost linear ascending branch in the STZ of specimen DS_S370_200_20_1, which was not present in the STZ of specimen DS_S370_200_20_1.

The higher strain capacity of the toughened adhesive allowed for achieving higher axial strain $\varepsilon(x)$ along the bonded length with respect to the traditional adhesive. This in turn determined a higher integral of shear stresses transferred along the bonded length for specimens with toughened than with traditional adhesives when the STZ was fully established, i.e., a higher bond capacity.

7.5. Effect of composite elastic modulus

The three specimens comprising the Type S CFRP plate showed the same cohesive failure in the adhesive layer exhibited by those reinforced with the Type M CFRP plate (Fig. 3). In both cases, the S370 toughened adhesive was employed. Although both series DS_S370_200 and DS_S370_S_200 were associated with the same $\tau(s)$ law and fracture energy [7], the Type M CFRP was characterized by a 22 % higher average elastic modulus than that of Type S (Table 1). As indicated in Table 2, specimens strengthened with the high-modulus composite provided a 14 % and 3 % higher values of $\overline{P}^*$ and $\overline{P}_u$, respectively, with respect to those of Type S specimens. A similar finding was presented in Ref. [7] for different types of FRP-steel adhesive joints and was confirmed analytically by Eq. (7), which provides the nonlinear relationship between the joint bond capacity and the composite plate elastic modulus (E_f).

Eq. (7) shows that increasing E_f the joint peak load increases. However, an increase in the composite elastic modulus entails for an increase in the effective bond length [see Eqs. (10)–(13)]. Thus, provided the same interface CML, a higher bonded length is needed to fully establish the STZ for a higher E_f than for a lower one.

7.6. Influence of the slip measuring technique

The load responses shown in Fig. 4a–e were obtained by considering the global slip g as the average measurements of LVDTs at the specimen loaded end. The global slip g can be also obtained by the 2D DIC measurements. Fig. 8 shows a comparison between the global slip measured by the LVDTs and that obtained by DIC analysis, for representative specimens of the three bonded lengths considered, namely DS_S370_200_20_1, DS_S370_100_20_3, and DS_S370_200_70_3. In Fig. 8, the global slip was obtained by DIC analysis as the difference between the average longitudinal (i.e., along the load direction) displacement of squares with size 5 pixel located at the loaded end, two on the composite strip and two on the steel support (see Fig. 8). Results in Fig. 8 showed that for $g < g^*$ the DIC generally provided a global slip lower than that obtained by the LVDTs for the same applied load. DIC

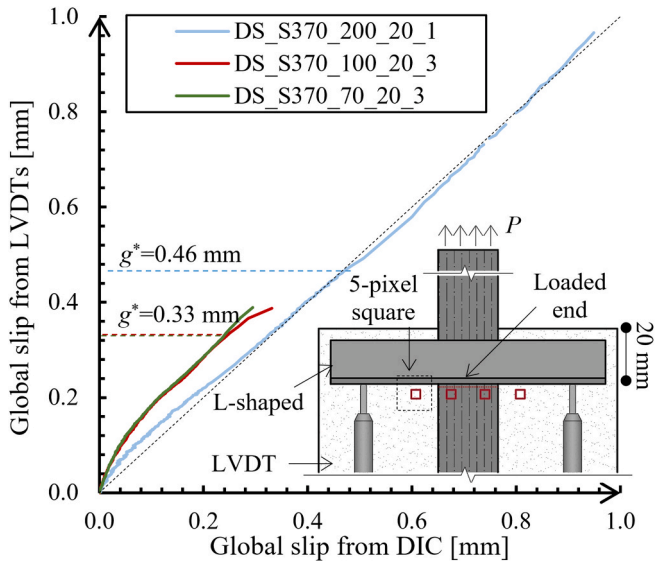

Fig. 8. Comparison between global slip measured by LVDTs and DIC.

measurements lower than corresponding LVDT measurements were already reported in the literature [50]. Furthermore, for the CFRP-steel joints in this paper, the difference between DIC and LVDT measurements can be also attributed to the eccentricity between the applied load and steel support restraint (Fig. 2b), which determined an out-of-plane rotation of the specimen. The DIC software could measure only the vertical component (i.e., on the orthogonal framing plane) of the displacement, whereas the LVDTs, being directly applied to the strengthened surface, followed its rotation. Therefore, the difference between LVDT and DIC measurements could be used to identify the specimen out-of-plane rotation. The global slips provided by LVDTs and DIC were similar at the beginning of the test and their difference became higher as the load increased, which indicated that the out-of-plane rotation angle varied during the test. This effect was more pronounced for specimens with short bonded length. For specimen DS_S370_200_20_1, the global slips provided by LVDTs and DIC were approximately equal after $0.87P^*$ was attained, which suggests a lower effect of the set-up eccentricity for specimens with high than with short bonded length.

8. Conclusions

In this paper, the bond behavior of CFRP-steel joints with toughened and traditional adhesives were experimentally investigated by performing single-lap direct shear tests. The parameters investigated were the type of adhesive, CFRP plate stiffness, and bonded length. Digital image correlation was used to capture the displacement field of the composite plate and compute corresponding axial strain distribution, which were then used to obtain the interface cohesive material law (CML). For some specimens, the full-range bond behavior was captured by controlling the direct shear test at the loaded and free ends of the CFRP-steel joint. An analytical model previously proposed by the authors was used to describe the results obtained and carefully compare the effect of the different parameters investigated. The results obtained allowed for drawing the following main conclusions.

- The toughened adhesive provided a tensile non-linear stress-strain behavior, whereas the traditional adhesive showed a linear elastic response. Furthermore, the former adhesive showed higher strain capacity with respect to that of the latter. This higher strain capacity resulted in a higher interface fracture energy of CFRP-steel joints with toughened adhesive than that of corresponding joints with traditional adhesive.
- The analytical model proposed accurately described the full-range bond behavior of CFRP-steel joints that showed a snap-back in the load response.
- Given the same adhesive type, the increase of the CFRP-steel joint bonded length provided an increase of the peak load until the bonded length reached the effective bond length and the bond capacity was attained. The effective bond length of CFRP-steel joints with toughened adhesive was higher than that of joints with traditional adhesive.
- Increasing the plate stiffness in CFRP-steel joints with the same bonded length and adhesive resulted in an increase of the peak load. However, the analytical model showed that a higher bonded length was needed to fully establish the STZ of CFRP-steel joints with toughened adhesive than with traditional adhesive.

CRediT authorship contribution statement

Angelo Savio Calabrese: Writing – original draft, Visualization, Methodology, Investigation, Data curation, Conceptualization. **Tommaso D'Antino:** Writing – original draft, Validation, Supervision, Resources, Conceptualization. **Pierluigi Colombi:** Writing – original draft, Validation, Supervision, Resources, Conceptualization.

Declaration of competing interest

The authors declare that they have no known competing financial interests or personal relationships that could have appeared to influence the work reported in this paper.

Data availability

Data will be made available on request.

Acknowledgements

The financial support of the Politecnico di Milano is gratefully acknowledged. Sika Services AG is acknowledged for providing the composites and adhesives. The authors express their gratitude to Mr. Daniele Spinelli of the Laboratorio Prove Materiali of the Politecnico di Milano for his precious help in conducting the free-end controlled tests.

References

[1] J.G. Teng, T. Yu, D. Fernando, Strengthening of steel structures with fiber-reinforced polymer composites, J. Constr. Steel Res. 78 (2012) 131–143, https://doi.org/10.1016/j.jcsr.2012.06.011.
[2] American Concrete Institute, Guide to Design and Construction of Externally Bonded FRP Systems for Strengthening Concrete Structures. ACI 440.2R-17, ACI, Farmington Hills, 48331 MI, 2017.
[3] M. Kamruzzaman, M.Z. Jumaat, N.H. Ramli Sulong, A.B.M.S. Islam, A review on strengthening steel beams using FRP under fatigue, Sci. World J. 2014 (2014) e702537, https://doi.org/10.1155/2014/702537.
[4] A. Hosseini, E. Ghafoori, M. Motavalli, A. Nussbaumer, X.-L. Zhao, R. Al-Mahaidi, et al., Development of prestressed unbonded and bonded CFRP strengthening solutions for tensile metallic members, Eng. Struct. 181 (2019) 550–561, https://doi.org/10.1016/j.engstruct.2018.12.020.
[5] L. Li, W. Wang, E. Chatzi, E. Ghafoori, Experimental investigation on debonding behavior of Fe-SMA-to-steel joints, Construct. Build. Mater. 364 (2023) 129857, https://doi.org/10.1016/j.conbuildmat.2022.129857.
[6] B. Zheng, M. Dawood, Fatigue crack growth analysis of steel elements reinforced with shape memory alloy (SMA)/fiber reinforced polymer (FRP) composite patches, Compos. Struct. 164 (2017) 158–169, https://doi.org/10.1016/j.compstruct.2016.12.077.
[7] T. Yu, D. Fernando, J.G. Teng, X.L. Zhao, Experimental study on CFRP-to-steel bonded interfaces, Compos. B Eng. 43 (2012) 2279–2289, https://doi.org/10.1016/j.compositesb.2012.01.024.
[8] C. Jiang, Q.-Q. Yu, X.-L. Gu, A unified bond-slip model for the interface between FRP and steel, Compos. B Eng. 227 (2021) 109380, https://doi.org/10.1016/j.compositesb.2021.109380.
[9] Y. Yang, H. Biscaia, C. Chastre, M.A.G. Silva, Bond characteristics of CFRP-to-steel joints, J. Constr. Steel Res. 138 (2017) 401–419, https://doi.org/10.1016/j.jcsr.2017.08.001.

[10] M. Bocciarelli, A new cohesive law for the simulation of crack propagation under cyclic loading. Application to steel- and concrete-FRP bonded interface, Theor. Appl. Fract. Mech. 114 (2021) 102992, https://doi.org/10.1016/j.tafmec.2021.102992.
[11] B. Wang, Y. Bai, X. Hu, P. Lu, Enhanced epoxy adhesion between steel plates by surface treatment and CNT/short-fibre reinforcement, Compos. Sci. Technol. 127 (2016) 149–157, https://doi.org/10.1016/j.compscitech.2016.03.008.
[12] Y. Hu, B. Yuan, F. Cheng, X. Hu, NaOH etching and resin pre-coating treatments for stronger adhesive bonding between CFRP and aluminium alloy, Compos. B Eng. 178 (2019) 107478, https://doi.org/10.1016/j.compositesb.2019.107478.
[13] M. Heshmati, R. Haghani, M. Al-Emrani, A. André, On the strength prediction of adhesively bonded FRP-steel joints using cohesive zone modelling, Theor. Appl. Fract. Mech. 93 (2018) 64–78, https://doi.org/10.1016/j.tafmec.2017.06.022.
[14] Y. Pang, G. Wu, H. Wang, D. Gao, P. Zhang, Bond-slip model of the CFRP-steel interface with the CFRP delamination failure, Compos. Struct. 256 (2021) 113015, https://doi.org/10.1016/j.compstruct.2020.113015.
[15] Y. Yang, J. Zhao, S. Zhang, C. Chastre, H. Biscaia, Effect of mechanical anchorage on the bond performance of double overlapped CFRP-to-steel joints, Compos. Struct. 267 (2021) 113902, https://doi.org/10.1016/j.compstruct.2021.113902.
[16] M. Liu, M. Dawood, A closed-form solution of the interfacial stresses and strains in steel beams strengthened with externally bonded plates using ductile adhesives, Eng. Struct. 154 (2018) 66–77, https://doi.org/10.1016/j.engstruct.2017.10.054.
[17] D. Fernando, T. Yu, J.G. Teng, Behavior of CFRP laminates bonded to a steel substrate using a ductile adhesive, J. Compos. Construct. 18 (2014) 04013040, https://doi.org/10.1061/(ASCE)CC.1943-5614.0000439.
[18] J. He, G. Xian, Bond-slip behavior of fiber reinforced polymer strips-steel interface, Construct. Build. Mater. 155 (2017) 250–258, https://doi.org/10.1016/j.conbuildmat.2017.08.062.
[19] Z. Wang, G. Xian, Cohesive zone model prediction of debonding failure in CFRP-to-steel bonded interface with a ductile adhesive, Compos. Sci. Technol. 230 (2022) 109315, https://doi.org/10.1016/j.compscitech.2022.109315.
[20] J.G. Teng, D. Fernando, T. Yu, Finite element modelling of debonding failures in steel beams flexurally strengthened with CFRP laminates, Eng. Struct. 86 (2015) 213–224, https://doi.org/10.1016/j.engstruct.2015.01.003.
[21] A.S. Calabrese, P. Colombi, T. D'Antino, Analytical solution of the full-range behavior of adhesively bonded FRP-steel joints made with toughened adhesives, Eng. Fract. Mech. 292 (2023) 109569, https://doi.org/10.1016/j.engfracmech.2023.109569.
[22] M. Bocciarelli, P. Colombi, T. D'Antino, G. Fava, Intermediate crack induced debonding in steel beams reinforced with CFRP plates under fatigue loading, Eng. Struct. 171 (2018) 883–893, https://doi.org/10.1016/j.engstruct.2018.04.002.
[23] M. Mohajer, M. Bocciarelli, P. Colombi, Calibration of a cyclic cohesive-zone model for fatigue-crack propagation in CFRP-strengthened steel plates, J. Compos. Construct. 26 (2022) 04022054, https://doi.org/10.1061/(ASCE)CC.1943-5614.0001243.
[24] T. Papa, M. Bocciarelli, A.S. Calabrese, P. Colombi, T. D'Antino, Experimental and numerical investigation of the bond behavior of CFRP-to-steel joints under fatigue loading. Proc. Of the 11th International Conference on Fibre-Reinforced Polymer (FRP) Composites in Civil Engineering, CICE 2023, International Institute for FRP in Construction (IIFC), Rio de Janeiro, 2023, https://doi.org/10.5281/zenodo.8164788.
[25] H.-T. Wang, G. Wu, Bond-slip models for CFRP plates externally bonded to steel substrates, Compos. Struct. 184 (2018) 1204–1214, https://doi.org/10.1016/j.compstruct.2017.10.033.
[26] H.-T. Wang, G. Wu, Y.-T. Dai, X.-Y. He, Experimental study on bond behavior between CFRP plates and steel substrates using digital image correlation, J. Compos. Construct. 20 (2016) 04016054, https://doi.org/10.1061/(ASCE)CC.1943-5614.0000701.
[27] H.-T. Wang, G. Wu, Y.-Y. Pang, J.-W. Shi, H.M. Zakari, Experimental study on the bond behavior between CFRP plates and steel substrates under fatigue loading, Compos. B Eng. 176 (2019) 107266, https://doi.org/10.1016/j.compositesb.2019.107266.
[28] P. Carrara, L. De Lorenzis, A coupled damage-plasticity model for the cyclic behavior of shear-loaded interfaces, J. Mech. Phys. Solid. 85 (2015) 33–53, https://doi.org/10.1016/j.jmps.2015.09.002.
[29] P. Colombi, M. Bocciarelli, A.S. Calabrese, T. D'Antino, T. Papa, Application of a toughened epoxy adhesive for the fatigue strengthening of steel structures, in: X.-L. Gu, M. Motavalli, A. Ilki, Q.-Q. Yu (Eds.), Proceedings of the 6th International Conference on Smart Monitoring, Assessment and Rehabilitation of Civil Structures, Springer Nature, Singapore, 2024, pp. 639–651, https://doi.org/10.1007/978-981-99-3362-4_51.
[30] Q.Q. Yu, T. Chen, X.L. Gu, X.L. Zhao, Z.G. Xiao, Fatigue behaviour of CFRP strengthened steel plates with different degrees of damage, Thin-Walled Struct. 69 (2013) 10–17, https://doi.org/10.1016/j.tws.2013.03.012.
[31] K.P. Unnikrishnan, E.T. Thachil, Toughening of epoxy resins, Des. Monomers Polym. 9 (2006) 129–152, https://doi.org/10.1163/156855506776382664.
[32] M.M. Shokrieh, S.M. Ghoreishi, M. Esmkhani, 11 - toughening mechanisms of nanoparticle-reinforced polymers, in: Q. Qin, J. Ye (Eds.), Toughening Mechanisms in Composite Materials, Woodhead Publishing, 2015, pp. 295–320, https://doi.org/10.1016/B978-1-78242-279-2.00011-1.
[33] Y. Kasper, M. Albiez, T. Ummenhofer, C. Mayer, T. Meier, F. Choffat, et al., Application of toughened epoxy-adhesives for strengthening of fatigue-damaged steel structures, Construct. Build. Mater. 275 (2021) 121579, https://doi.org/10.1016/j.conbuildmat.2020.121579.
[34] T. Meier, F. Choffat, A. Montalbano, Toughened 2K-epoxy adhesives: structural strengthening of steel structures. IABSE Congress, Christchurch 2020: Resilient Technologies for Sustainable Infrastructure - Proceedings, 2020, pp. 898–902, https://doi.org/10.2749/christchurch.2021.0898.
[35] Sika Italia S.p.A. Technical Datasheet of Sika CarboDur M, 2021.
[36] Sika Italia S.p.A. Technical Datasheet of Sika CarboDur S, 2021.
[37] European Committee for Standardization. EN ISO 527-4:2021, Plastics - Determination of Tensile Properties. Part 4: Test Conditions for Isotropic and Orthotropic Fibre-Reinforced Plastic Composites, 2022.
[38] Sika Italia S.p.A. Technical Datasheet of Sikadur 30, 2022.
[39] ASTM International. ASTM D638-22, Standard Test Method for Tensile Properties of Plastics, 2022.
[40] H. Yuan, J.G. Teng, R. Seracino, Z.S. Wu, J. Yao, Full-range behavior of FRP-to-concrete bonded joints, Eng. Struct. 26 (2004) 553–565, https://doi.org/10.1016/j.engstruct.2003.11.006.
[41] Z. Wu, H. Yuan, H. Niu, Stress transfer and fracture propagation in different kinds of adhesive joints, J. Eng. Mech. 128 (2002) 562–573, https://doi.org/10.1061/(ASCE)0733-9399(2002)128:5(562.
[42] A.S. Calabrese, T. D'Antino, P. Colombi, Experimental and analytical investigation of PBO FRCM-concrete bond behavior using direct and indirect shear test set-ups, Compos. Struct. 267 (2021), https://doi.org/10.1016/j.compstruct.2021.113672.
[43] L. De Lorenzis, G. Zavarise, Interfacial stress analysis and prediction of debonding for a thin plate bonded to a curved substrate, Int. J. Non Lin. Mech. 44 (2009) 358–370, https://doi.org/10.1016/j.ijnonlinmec.2009.01.002.
[44] M.A. Sutton, J.-J. Orteu, H.W. Schreier, Image Correlation for Shape, Motion and Deformation Measurements: Basic Concepts, Theory and Applications, Springer, New York, N.Y, 2009.
[45] M. Zhu, T. Ueda, J.-H. Zhu, Generalized evaluation of bond behavior of the externally bonded FRP reinforcement to concrete, J. Compos. Construct. 24 (2020) 04020066, https://doi.org/10.1061/(ASCE)CC.1943-5614.0001081.
[46] P. Carrara, D. Ferretti, F. Freddi, G. Rosati, Shear tests of carbon fiber plates bonded to concrete with control of snap-back, Eng. Fract. Mech. 78 (2011) 2663–2678, https://doi.org/10.1016/j.engfracmech.2011.07.003.
[47] Z.P. Bažant, J. Planas, Fracture and Size Effect in Concrete and Other Quasibrittle Materials, CRC Press, Boca Raton, 1998.
[48] A.S. Calabrese, P. Colombi, T. D'Antino, Analytical solution of the bond behavior of FRCM composites using a rigid-softening cohesive material law, Compos. B Eng. 174 (2019) 1–10, https://doi.org/10.1016/j.compositesb.2019.107051.
[49] J. Dai, T. Ueda, Y. Sato, Unified analytical approaches for determining shear bond characteristics of FRP-concrete interfaces through pullout tests, J. Adv. Concr. Technol. 4 (2006) 133–145, https://doi.org/10.3151/jact.4.133.
[50] M. Santandrea, I.A.O. Imohamed, C. Carloni, Width effect in FRP–concrete debonding mechanism: a new formula, J. Compos. Construct. 24 (2020) 04020024, https://doi.org/10.1061/(ASCE)CC.1943-5614.0001001.